



Research Article

Fractal Characteristics and Acoustic Emission during the Failure Process of Argillaceous Siltstone with Different Moisture Contents

Haoran Song ¹, Shouyu Li,¹ Jiachen Xu,¹ Qingwen Zhang ¹ and Yonghui Zhi^{2,3}

¹College of Civil Engineering, Southwest Forestry University, Kunming 650224, China

²China Railway Development investment Group Co., Ltd., Kunming 650200, China

³The 5th Engineering Co., Ltd. of China Railway 1 Bureau Group Corporation, Baoji 721006, China

Correspondence should be addressed to Qingwen Zhang; 99tmzqw@swfu.edu.cn

Received 22 October 2022; Revised 28 December 2022; Accepted 29 December 2022; Published 10 January 2023

Academic Editor: Yu Wang

Copyright © 2023 Haoran Song et al. This is an open access article distributed under the Creative Commons Attribution License, which permits unrestricted use, distribution, and reproduction in any medium, provided the original work is properly cited.

Compressive strength and tensile strength are the critical parameters to determine rock performance, which can reflect the rock's resistance to deformation and damage. Brazilian indirect tensile and uniaxial compression tests were carried out on rocks under different water immersion conditions to study acoustic emission (AE) characteristics and crack propagation during rock fracture. The test results show that water has a deteriorating effect on the argillaceous siltstone, with significant attenuation of both compressive and tensile strengths. With the increase in moisture content, the number of AE events decreased, the cumulative AE ringing count showed a gradual rise in steps, and the proportion of AE peak frequencies in the range of 0-200 kHz gradually increased. Natural rock samples are more brittle than water-saturated rock samples. The higher frequency of AE events and the higher energy released during the destruction of natural rock samples reflect in the clustering of high-energy AE source locus near the main rupture surface. The AE source locus is 1-2 energy levels higher in the vicinity of the fracture surface than in the water-saturated rock samples. The rock samples exhibited random packing of mineral particles and contained many clay minerals by SEM analysis of fracture microstructure. Water dissolves mineral particles and cementitious materials, producing microcracks with propagation potential. Analysis of the AE time sequence based on fractal theory reveals that fractal dimension value varies with the increase of moisture content. The variation of the fractal dimension D values for the water-saturated rock samples ranges from 0.4 to 0.65. This indicates that the number of microcracks is higher and their propagation more complex when the moisture content of the specimen is higher. The failure characteristics of the rock samples in the above research can provide a reference for monitoring rock mass stability under tunnel water inflow.

1. Introduction

As the mining of mine resources gradually moves towards the construction of tunnel projects such as highways and railways, the geological environment faced by rock mass engineering is becoming more and more complex [1, 2]. In tunnel excavation, the rock mass is usually in a state of compression and partially in a state of tension. The instability failure of rock mass is mainly caused by the expansion and penetration of internal cracks [3]. Groundwater exists in rock mass engineering, and water infiltration also weakens its mechanical properties and stability. Water plays a vital

role in rocks' mechanical properties and damage [4]. Therefore, studying the development of internal cracks during the destabilization of water-saturated rocks is essential for understanding the destabilization mechanism of water-rich rock masses.

Previous scholars have done a lot of research on rock failure forms under different loading methods. In the uniaxial compression test, the sandstone specimens mainly failed centrally or after multiple types of fracturing. The nature of the dominant failure mode varied from axial splitting to shearing along a single plane to multiple fractures [5]. Wu et al. [6] analyzed sandy mudstone's mechanical properties,

crack propagation characteristics, and failure characteristics under uniaxial compression, Brazilian splitting, and type I fracture toughness. Okub et al. [7] conducted uniaxial compression, Brazilian splitting, and direct tensile tests on anthracite under different loading rates. They studied the deformation and failure characteristics of anthracite under other loading methods.

Many scholars have presented research on the AE features during the processes of rock fractures. The closure of the original microcracks in the rock, initiation, expansion, and penetration of new cracks will lead to the damage and destruction of the rock and the acoustic waves of different frequencies and different energies induced by the microcracks in the evolution process, namely, the acoustic emission (AE) of the rock [8–11]. The AE signal contains complete information on the rock damage evolution process, which can reflect the rock damage accumulation process [12] and is widely used in monitoring and predicting the stability and safety of the underground rock mass [13–16]. Many scholars have studied the characteristics of AE during rock fracture in various test types. Wang et al. [17] used the AE detection system to learn the stress wave caused by crack initiation and propagation of red sandstone samples to analyze and evaluate the rock fracture process. Zhang et al. [18] studied the characteristics of shale in different lamination directions and loading directions and explored the mechanical properties and damage modes of shale. Cheon et al. [19] developed a new type of AE signal monitoring device to evaluate the deformation and damage of rock slopes according to the characteristics of AE parameters. The AE localization technique is used to characterize the entire progressive failure process of rocks with preexisting fractures and to study the propagation process and AE characteristics of different types of cracks [20–23]. The scholars' efforts above provided valuable information for understanding the relationship between crack propagation mechanisms and acoustic emission signal parameters during rock fracture.

The theory of fractal dimension can also be used to understand the rock damage process and crack propagation mechanisms. Kusunose et al. [24] took granite with different texture distributions as the research object, analyzed the fractal dimension patterns of the spatial distribution of AE events, and concluded that the rock structure might affect the growth of internal microcracks and the distribution of AE events. Based on the basic theory of fractal geometry, Xie et al. [25] proposed a column-covering method to analyze the fractal characteristics of AE spatial distribution during rock damage and failure, which can be based on stress reduction, energy release, and AE spatial distribution fractal dimensionality to predict the failure state of rocks. Biancolini et al. [26] used the boxed fractal dimension to determine better the crack formation and propagation condition, which can be used to predict cracks' propagation and evolution. Zhang et al. [27] conducted uniaxial and triaxial experiments on granite using AE positioning technology and studied the fractal characteristics of AE temporal and spatial distribution development. It was found that with the increase in stress level, the fractal dimension of time distri-

bution showed a “rising-falling” pattern, and the fractal dimension of space showed a “decreasing” way.

However, the previous studies mentioned above generally focused on the macroscopic crack propagation mechanisms and AE characteristics of a type of natural rock under a specific loading condition. Studies that systematically analyze the effect of moisture content on rock properties, AE characteristics, and microscopic crack propagation mechanisms still need to be made available. Rock is an anisotropic nonlinear material, and its inelastic properties are determined by many factors such as stress state, strain rate, microstructure, temperature, and moisture content [28–30]. Among many factors, moisture content has a noticeable effect on the deterioration of rock. Compared with previous studies, this paper uses the universal testing machine system, the strain displacement video measurement system, and the acoustic emission monitoring system to carry out uniaxial and splitting experiments on the red-bed argillaceous siltstone in central Yunnan. The deformation and failure characteristics, acoustic emission evolution patterns, and microscopic failure mechanisms of water-saturated and natural rock samples are compared and analyzed. In addition, this study also analyzes the spatial distribution mode of acoustic emission, fractal dimension characteristics, and the influence of moisture content on the acoustic emission characteristics. It explores the crack propagation mechanisms of argillaceous siltstone under different moisture content. The results of this study expect to deepen our understanding of the assessment of surrounding rock stability under tunnel water inflow conditions.

2. Materials and Methods

2.1. Rock Specimens. “Central Yunnan Red Layer” refers to the continental clastic sedimentary strata mainly distributed in Chuxiong, Yuxi, Dali Xiangyun, and other areas in Yunnan, formed from the Late Triassic to the Paleocene, and the appearance is primarily red. The argillaceous siltstone used in this study is taken from a diversion tunnel excavated in the red bed of Xiangyun County, Yunnan Province, Western China. The argillaceous siltstone was examined by X-ray diffraction (XRD) to determine its mineral composition (Figure 1), which showed mainly quartz (70%), calcite (5%), hydromica/illite (10%), plagioclase (5%), kaolinite (5%), and chlorite (5%). Its density is 2571–2677 kg/m³, porosity is 6.18–6.22%, internal friction angle is 45.65–47.86°, and cohesion is 7.47–7.83 MPa.

The chemical composition of argillaceous siltstone is mainly composed of oxides of silicon, aluminum, calcium, magnesium, potassium, and iron, among which silica content is the highest, accounting for more than half. It exists in complex clay minerals, primary silicate minerals, and free silicon oxide. Alumina is an essential component of clay mineral complexes and primary silicates. Calcium oxide mainly exists in the form of carbonate. Iron oxide is the main component affecting rock color. Potassium oxide is a component of hydromica adsorbed by clay minerals in the form of potassium ions. The argillaceous siltstone contains clastic minerals dominated by quartz and clay minerals

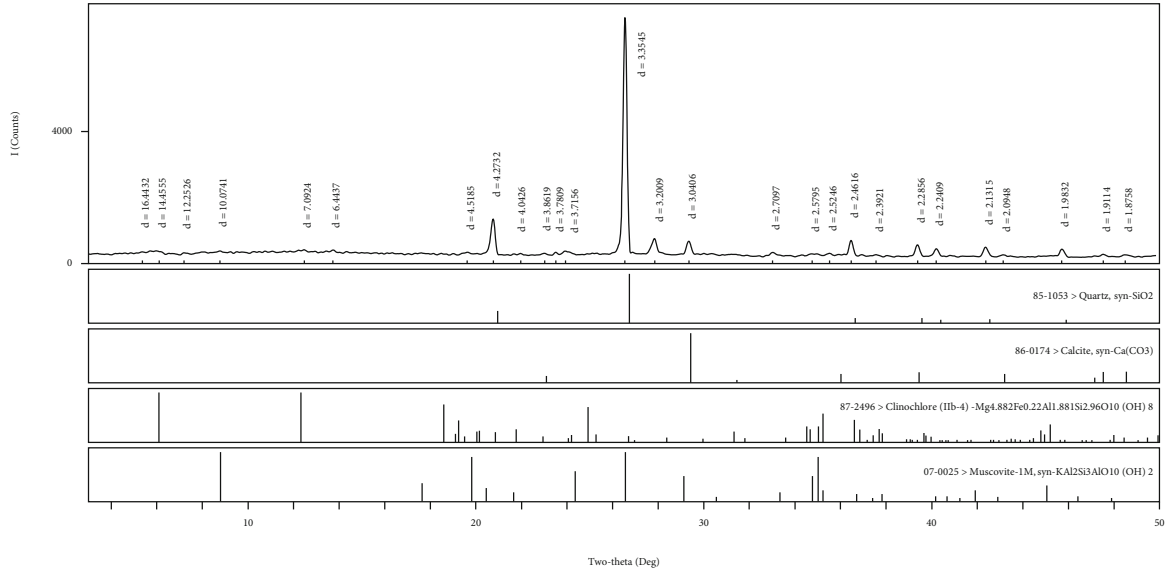


FIGURE 1: XRD analysis of argillaceous siltstone material in this research.

dominated by illite, kaolinite, and chlorite. Clay minerals have the characteristics of a large surface area, strong hydrophilicity, and large ion exchange capacity. Therefore, the deterioration of argillaceous siltstone by water is noticeable [31].

The purpose of this research is to study the effect of moisture content on the strength and AE fractal characteristics of argillaceous siltstone by uniaxial compression test and Brazilian indirect tensile test. The samples were prepared as standard cylindrical specimens with a height of 100 mm and a diameter of 50 mm and standard disc-shaped specimens with a height of 25 mm and a diameter of 50 mm (Figure 2(d)). The sample's surface is carefully polished so that the surface flatness is controlled below 0.02 mm. Bake the sample in an oven at 105°C for 24 hours, and record the quality of the sample after drying. In order to obtain the samples in four hydrated states, the samples were naturally saturated with four different immersion times, namely, 0 h, 24 h, 72 h, and 168 h (saturated). Number the samples of different water-containing states and record the quality of the samples after immersion. The measured moisture content results are shown in Table 1. A random speckle pattern was created on the surface of the specimen with matte white spray paint and a black marker for better DIC analysis. Check the integrity and uniformity of the samples after immersion before testing.

2.2. Testing Apparatus. Uniaxial compression tests and Brazilian indirect tensile tests were performed on the argillaceous siltstone samples using an electrohydraulic servo test system (model: CSS-WAW-600) (Figure 2(a)). The bearing capacity and bearing accuracy of the test system are 600 kN and 1%, respectively. The DS5 full-information acoustic emission signal analysis system was used in this study (Figure 2(b)). During signal acquisition, the preamplifier gain was set to 40 dB, the threshold was set to 100 mV, and the sampling rate was 5 MHz. The noise is filtered with a

hardware analog filter (the lower frequency is set to 100 kHz, and the upper frequency is set to 400 kHz). The XTDIC full-field strain measurement analysis system was also used in the study (Figure 2(b)). A German (model: Basler acA2440-75um) black-and-white industrial camera for visual monitoring was used, equipped with a 25 mm lens, to collect the artificial speckle pattern on the surface of the sample during the loading process at five frames per second (Figure 2(c)), with an image resolution of 2 448 × 2 048 pixels.

2.3. Test Methods. In order to obtain an effective and stable crack propagation, the axial loading method uses axial stress control. The uniaxial compression test adopts the method of graded loading. When the axial stress increases to a stress step at a rate of 0.5 MPa per second, the stress is held at that level for a period of time. The axial stress is then further increased at a rate of 0.5 MPa per second and held again for a certain time. Repeat the loading step until the rock breaks. For the Brazilian indirect tensile test, a nonlinear loading method was used, and the loading rate was 0.02 MPa per second. The treated disk sample is placed in a special fixture, and the fixture is a 30° metal gasket to achieve the purpose of nonlinear loading. The acoustic emission sensor is coated with a layer of couplant to strengthen the contact between the sensor and the rock and to ensure the integrity of the acoustic emission signal. For each test, the camera and acoustic emission monitoring system are triggered simultaneously with the loading device, and all test data are automatically recorded by the computer.

3. Experimental Results and Theoretical Analysis

3.1. AE Count Characteristics. The AE ringing count can reflect the intensity and frequency of rock activity in the test. The AE ringing count was used to compare and analyze the

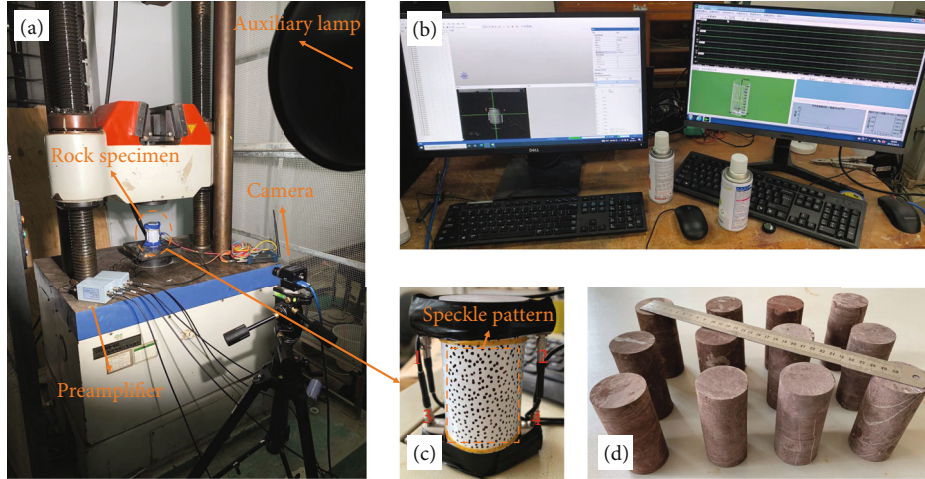


FIGURE 2: (a) Photo of the test setup. (b) DIC desktop (left) and AE desktop (right). (c) Argillaceous siltstone with speckle pattern and the locations of the attached AE sensors (from 1 to 4). (d) Argillaceous siltstone specimens.

TABLE 1: Moisture content of argillaceous siltstone at different soaking times.

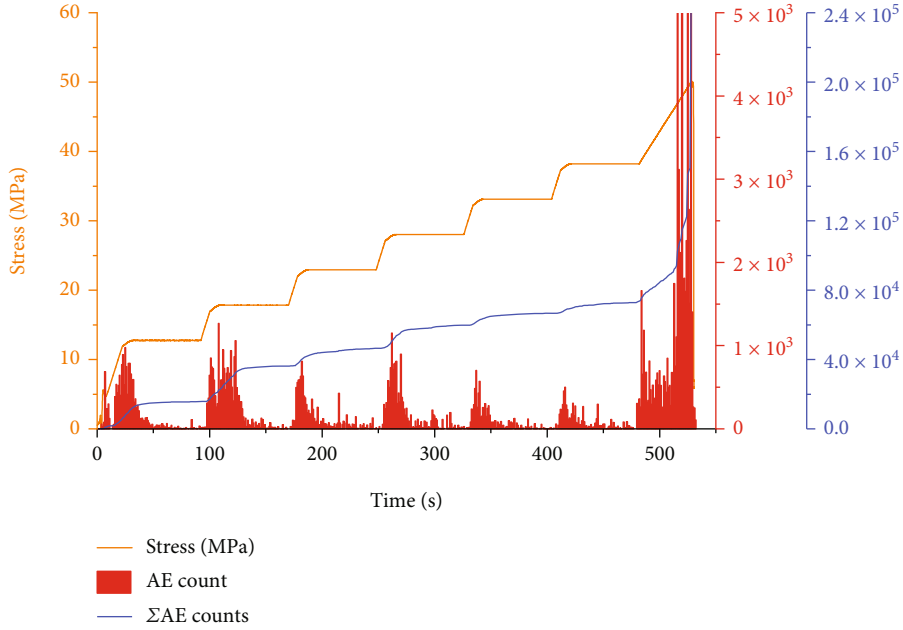
Rock specimen	Soaking time (h)	Soaking quality (g)	Drying quality (g)	Poor quality (g)	Moisture content (%)	Average moisture content (%)
U0-1	0	452.77	451.24	1.53	0.3391	0.3384
U0-2		463.46	461.91	1.55	0.3356	
T0-1		120.30	119.90	0.40	0.3336	
T0-2		118.71	118.30	0.41	0.3454	
U1-1	24	463.63	461.54	2.09	0.4528	0.4945
U1-2		423.90	421.71	2.19	0.5193	
T1-1		120.33	119.71	0.62	0.5179	
T1-2		118.50	117.92	0.58	0.4880	
U3-1	72	467.47	460.30	5.17	1.1183	1.0278
U3-2		473.56	468.99	4.57	0.9744	
T3-1		122.52	121.34	1.18	0.9725	
T3-2		119.81	118.57	1.24	1.0458	
U7-1	168	484.07	477.36	6.71	1.4056	1.7292
U7-2		472.45	464.02	8.43	1.8167	
T7-1		121.59	119.42	2.17	1.8171	
T7-2		120.48	118.26	2.22	1.8772	

rock samples in the uniaxial compression test and the Brazilian indirect tensile test under different moisture contents. Select representative rock samples with similar average moisture content: U0-1, U1-2, U3-2, U7-2, T0-1, T1-2, T3-2, and T7-1. To make the ringing count curve clearer and to facilitate the analysis of parameter variation patterns, the maximum value of ringing counts per second is set to a uniform 5 000.

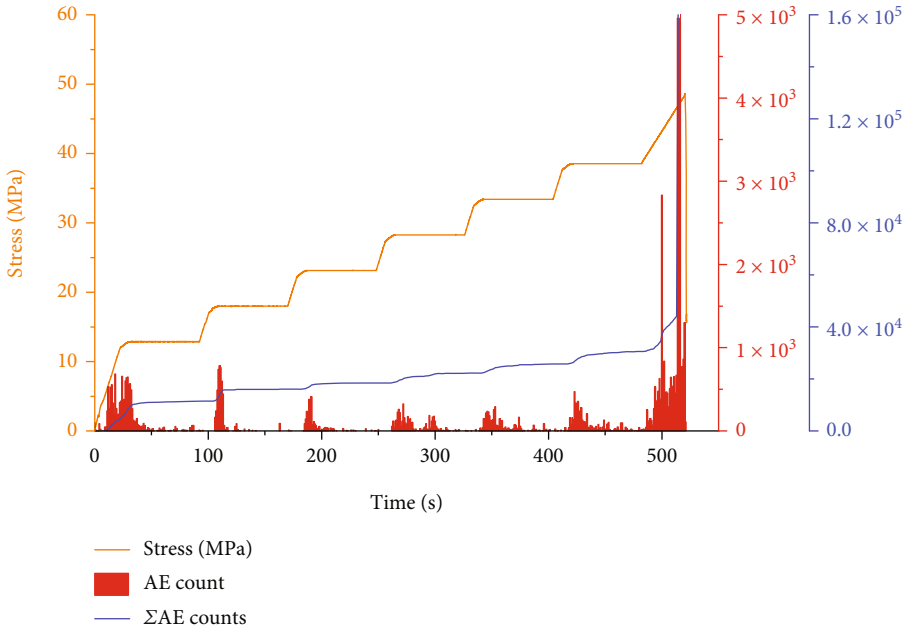
As shown in Figure 3(a), at the beginning of each stage of grading loading of the natural rock sample U0-1, the primary cracks were compacted and started to close under the action of stress, the acoustic emission ringing counts were more active, and there was a period of accumulation of ringing counts. When the stress stabilized, the AE ringing count dropped sharply and remained deficient, and the cumulative ringing count increased gradually. There is an apparent rise

in the cumulative ringing count, increasing stress at each level. When gradually loaded to the failure stress, the cracks in the rock begin to expand and penetrate, and the frequency of AE activity surges. During failure, the rock sample cracked concisely, and accompanied by a loud noise, the axial stress dropped rapidly, and the accumulated ringing count quickly jumped. At this time, the maximum value of the ringing count reached 104 618. In the loading stage before the peak, the average ringing count was 285.33, accounting for 0.30% of the maximum ringing count, and the cumulative ringing count was 150 369, accounting for 58.51% of the total count.

As shown in Figures 3(b)–3(d), the water-soaked rock samples were soaked in water for 24 h, 72 h, and 168 h, respectively. The rock sample soaked for 168 h contrasts with the natural rock sample. The moisture content of the

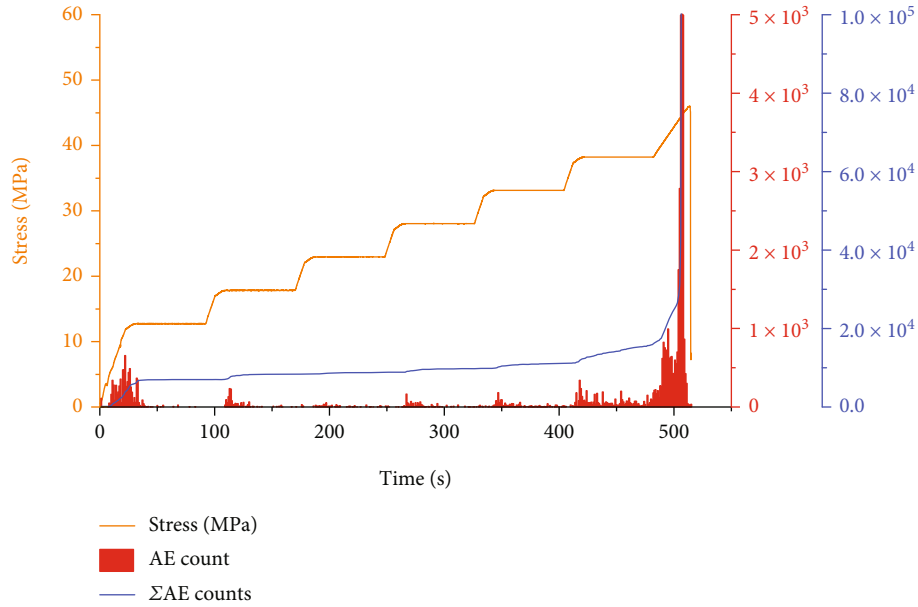


(a) U0-1

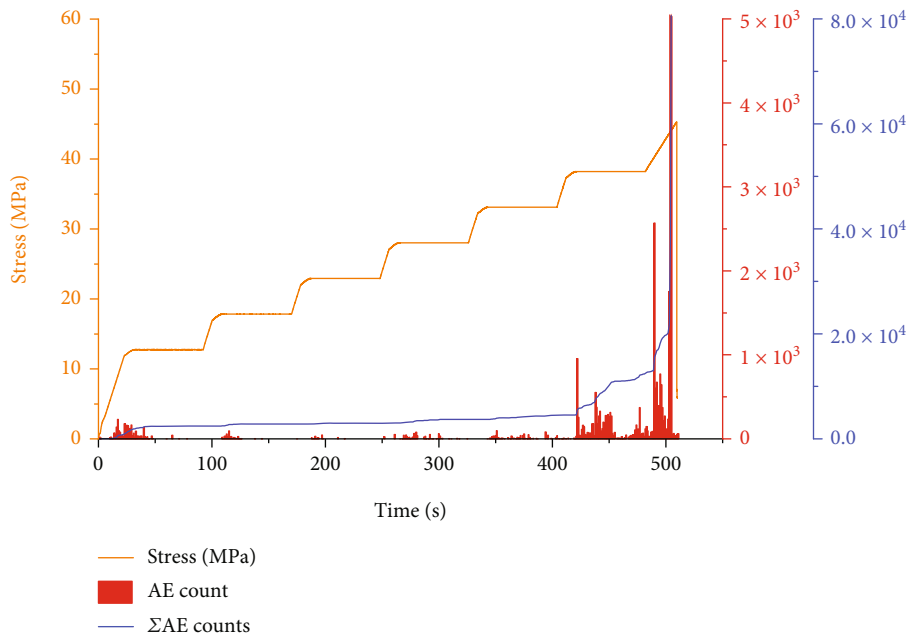


(b) U1-2

FIGURE 3: Continued.



(c) U3-2



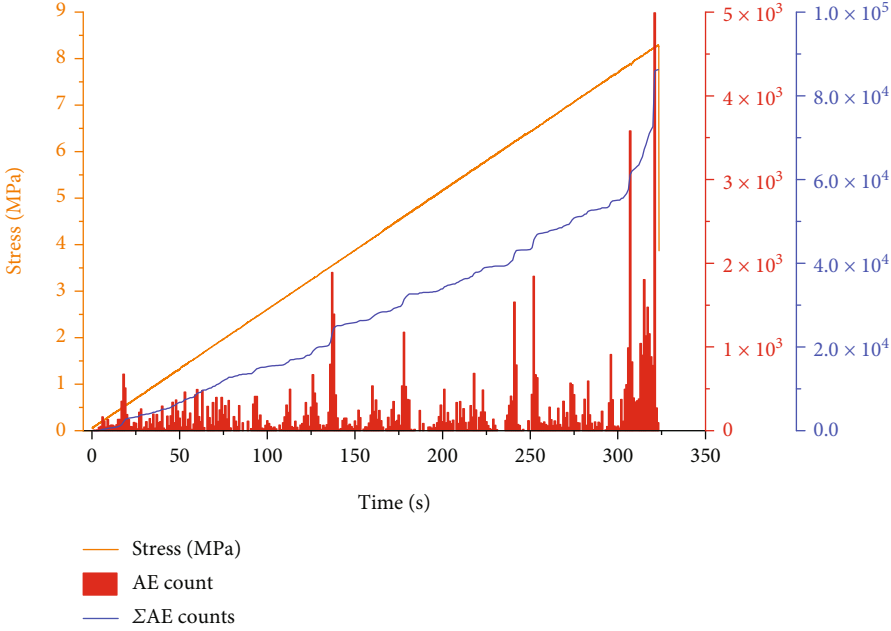
(d) U7-2

FIGURE 3: Relationships of stress, AE counts, and cumulative AE counts with time in the uniaxial compression test for different moisture contents.

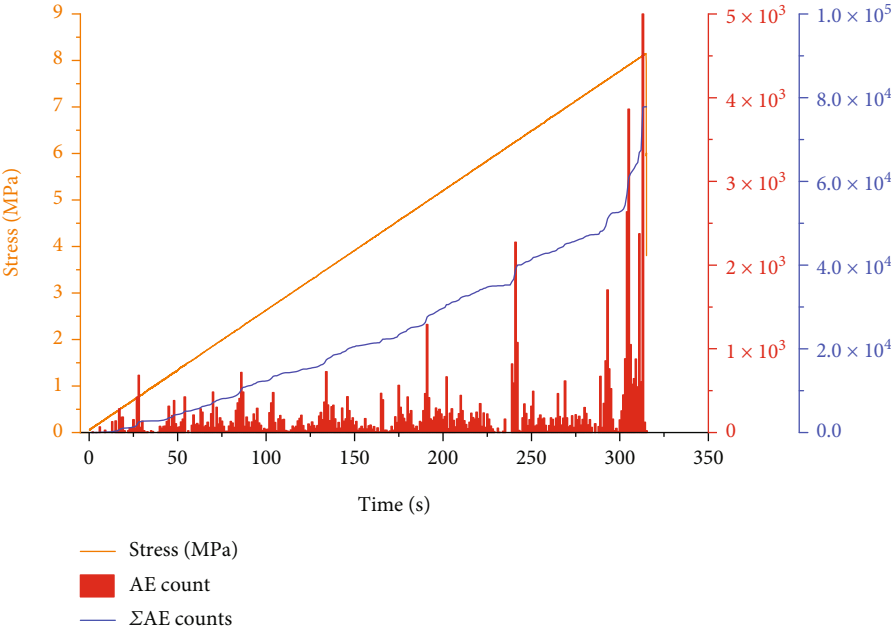
rock sample is 1.8772%, the AE activity is less in the stage of grading loading, and the cumulative ringing count has no prominent rise. The graded loading resulted in stable crack propagation and less strength decay in the soaked rock samples. Due to the attenuation of the strength of the rock sample, the sound is dull when it is destroyed. The total counts of rock samples in Figures 3(b)–3(d) are 239 355, 223 028, and 107 510, respectively, 96.90%, 90.29%, and 43.52% of the total counts of natural rock samples, respectively. Natural rock samples have intact skeletal particles with strong internal cementation and friction, and the propagation of

microcracks generates more acoustic emission signals. The water-rock chemistry of the clay minerals within the soaked rock samples weakens the cohesive forces between the skeletal particles. The reduction in misalignment between mineral crystals results in less acoustic emission signal with elevated loading stress in soaked rock samples. With the increase in moisture content, the growth of the cumulative ringing count gradually slowed down, and the cumulative ringing count jumped almost vertically before the destruction.

As shown in Figures 4(a)–4(d), in the Brazilian indirect tensile test, the tensile strength decays with increasing

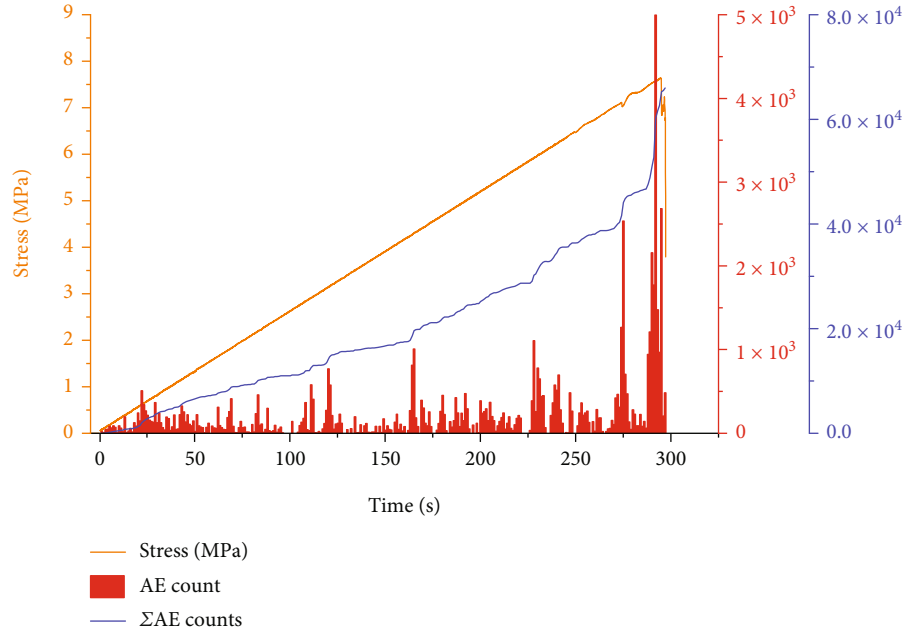


(a) T0-1

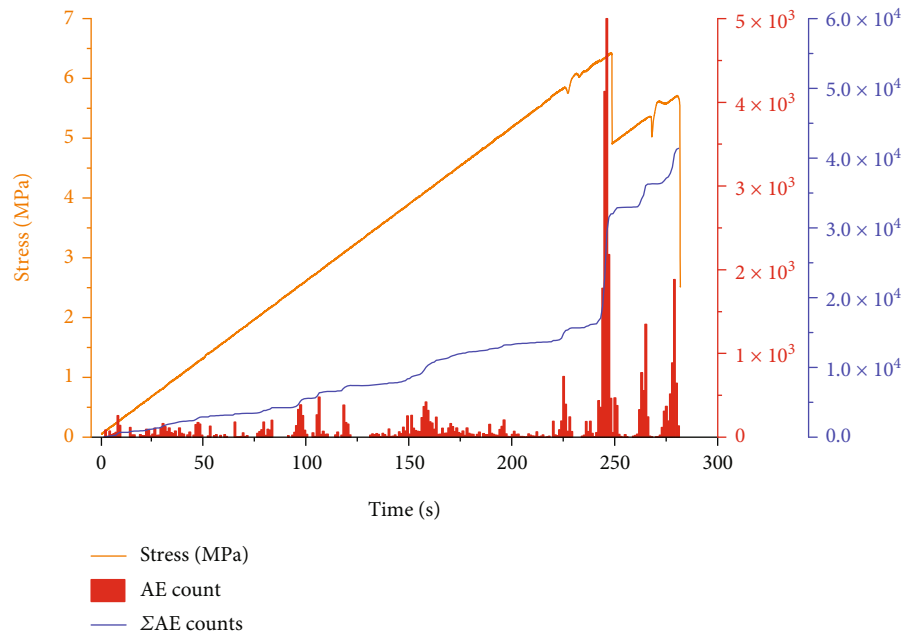


(b) T1-2

FIGURE 4: Continued.



(c) T3-2



(d) T7-1

FIGURE 4: Relationships of stress, AE counts, and cumulative AE counts with time in the Brazilian indirect tensile test for different moisture contents.

moisture content. Compared with the natural rock sample T0-1, the tensile strength of the water-soaked rock sample T7-1 lost 36.44%. The stress curve decreases after the load peaks and then begins to increase slightly but does not exceed the original peak stress. The AE ringing count curves exhibited by the split failure of rocks with different moisture contents are different. When the moisture content is low ($<1.0458\%$), the growth of the ringing count curve gradually becomes gentle with the increase of the moisture content, and the cumulative acoustic emission ringing count curve

shows a quasilinear upward trend. When the moisture content is high ($>1.0458\%$), the acoustic emission ringing count decreases, and the ringing count curve rises smoothly in steps. The acoustic emission ringing counts were uniformly distributed throughout the stages of the Brazilian splitting test, and there was no apparent quiet period, indicating that the cracks inside the rock expanded steadily with increasing loads. Comparing the natural rock sample with the water-soaked rock sample, the maximum ringing count of the natural rock sample is 13 229, and the accumulated ringing

count is 86 254. The maximum ringing counts of the water-soaked rock samples are 10 088, 7 356, and 6 340, accounting for 76.26%, 55.61%, and 47.93% of the natural rock samples, and the cumulative ringing counts are 77 108, 65 407, and 41 122, accounting for 89.40%, 75.83%, and 47.68% of the natural rock samples.

3.2. AE Peak Frequency. The acoustic emission peak frequency characteristic is analyzed by the peak frequency of the acoustic emission signal collected by the sensors. The comparison chart of the acoustic emission peak frequency distribution of the uniaxial compression test and the Brazilian indirect tensile test under four different moisture contents is shown in Figures 5(a) and 5(b). The AE peak frequencies of both test types are almost distributed below 400 kHz. In the uniaxial compression test, the AE peak frequency is mainly concentrated in 0-100 kHz, and the proportion of AE peak frequency in this range gradually increases with the increase of moisture content. In the Brazilian indirect tensile test, the peak frequency of AE is mostly higher than 100 kHz and mainly concentrated in the range of 200-400 kHz. With the increase in moisture content, the proportion of AE peak frequency in the range of 0-200 kHz gradually increased, while the proportion of AE peak frequency in the range of 300-400 kHz gradually decreased. The distribution of AE peak frequencies is determined by how the cracks propagate inside the rock sample. The high crack propagation velocity and low propagation scale cause the high AE peak frequency. Tensile cracks usually have a higher propagation velocity and lower propagation scale than shear cracks, but shear cracks are generally the penetrating failure of macroscopic cracks. The water moisture inside the rock sample increases, the rapid expansion of microcracks decreases, and the penetration failure of macrocracks increases, so the proportion of AE peak frequency in the low range gradually increases.

3.3. AE Location and Spatial Evolution Characteristics. During the deformation and failure of rock samples, energy is released to the surrounding in the form of elastic waves (acoustic emission). By analyzing the acoustic emission signal and the acoustic emission positioning point, the analysis of the evolution process of crack initiation, propagation, and penetration failure in the rock sample can be realized. In order to investigate the effect of moisture content on the deterioration of rock samples, a natural rock sample group and a water-saturated group soaked for 168 h were selected for comparative analysis. According to the evolution characteristics of acoustic emission parameters and the time-stress-ringing count curve, the grading loading of rock under uniaxial compression is divided into four processes: compaction stage, elastic stage, plastic stage, and failure stage. As shown in Figures 6-8, the position of the point represents the AE positioning source, and the color of the point from green, yellow, and orange to red represents the energy release of the positioning source from low to high.

For the uniaxial compression test, the pictures of the rock samples at each stage in Figures 6(e)-6(h) and 7(e)-7(h)

correspond to the AE localization sources in Figures 6(a) and 6(b) and 7(a) and 7(b):

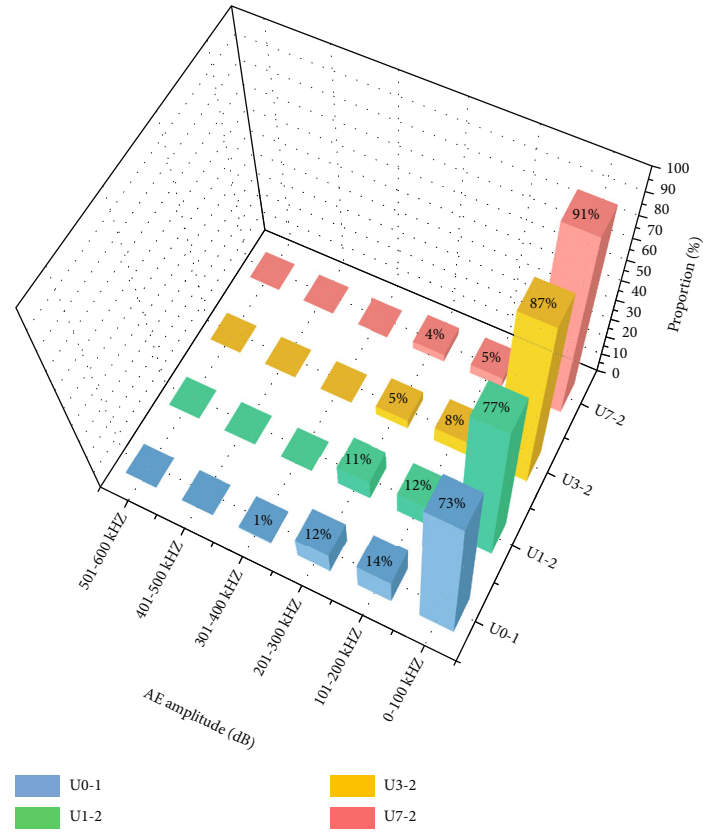
During the compaction stage (Figures 6(a) and 6(e) and 7(a) and 7(e)), the positioning points of rock sample U0-1 (accounting for 15.38% of the whole stage) are distributed at both ends of the specimen. There are many positioning points at the bottom and some yellow AE sources where microcracks generate. The number of positioning points of rock sample U7-2 (accounting for 11.87% of the whole stage) is much lower than that of U0-1, and green AE sources scatter at the end of the specimen.

During the elastic stage (Figures 6(b) and 6(f) and 7(b) and 7(f)), the positioning points of rock sample U0-1 (accounting for 21.46% of the whole stage) are concentrated in the lower half of the specimen and begin to spread to the middle of the specimen, and the microcracks expand into small-scale cracks. The yellow AE sources and a large number of green AE sources are linearly distributed up the crack and have the potential to expand. Due to the gradual increase of stress, new microcracks began to occur, and some of the yellow AE source localization points were concentrated on the left side of the specimen. The positioning points of rock sample U7-2 (accounting for 20.20% of the whole stage) are distributed at both ends of the specimen. The distribution of yellow AE sources and green AE sources is relatively uniform.

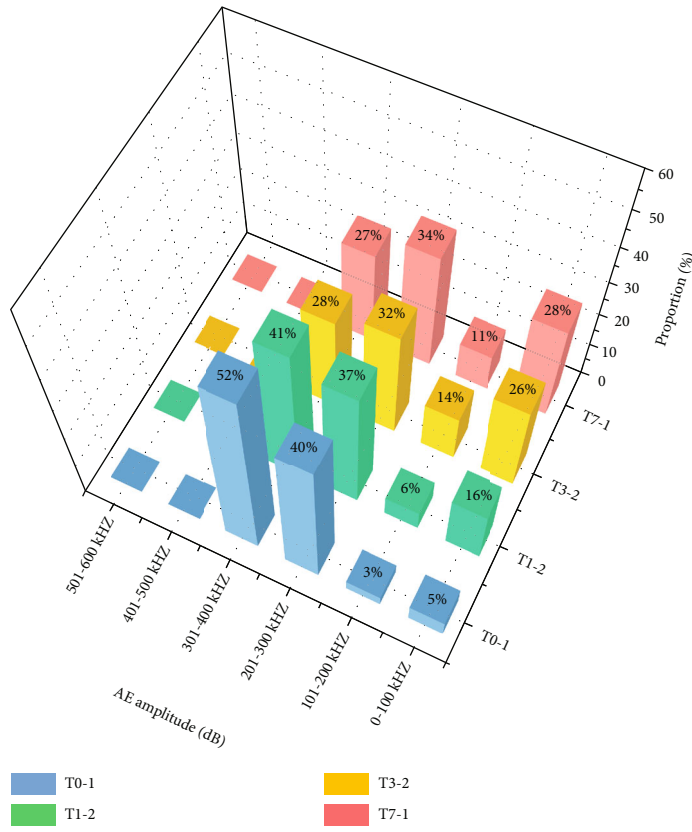
During the plastic stage (Figures 6(c) and 6(g) and 7(c) and 7(g)), the positioning points of rock sample U0-1 (accounting for 29.18% of the whole stage) concentrate in the middle part of the specimen, and a high-level AE source appears. Small-scale cracks extended from bottom to top and penetrated the entire specimen to form large-scale cracks, causing severe damage to the interior of the rock sample. The positioning points of rock sample U7-2 (accounting for 27.53% of the whole stage) are mainly distributed at the specimen's upper end and produce many microcracks.

During the failure stage (Figures 6(d) and 6(h) and 7(d) and 7(h)), the positioning points of rock sample U0-1 (accounting for 33.98% of the whole stage) are still concentrated around large-scale cracks with severe damage. The shear failure occurred inside the rock sample, and large-scale cracks rapidly expanded into a macroscopic damaged surface. The positioning points of rock sample U7-2 (accounting for 40.4% of the whole stage) showed a sudden and large increase, and the microcracks at the upper end of the rock sample expanded into large-scale cracks and extended downward to form a damaged surface.

For the Brazilian indirect tensile test (Figures 8(a) and 8(b)), the cracks in the early stage of the test loading are usually fast, and small-scale expansion and the released energy are low. Therefore, the middle and later stages with higher released energy are selected for analysis. The positioning points of the rock sample T0-1 distribute along the damaged surface formed by the tensile stress, and the failure surface evenly penetrates the entire specimen along the central axis. Two red AE sources, four orange AE sources, and a large number of yellow AE sources cluster in the middle of the fracture surface, and the AE sources extend to the upper



(a) Uniaxial compression test



(b) Brazilian indirect tensile test

FIGURE 5: Comparisons of AE peak frequency distributions. (a) Uniaxial compression test. (b) Brazilian indirect tensile test.

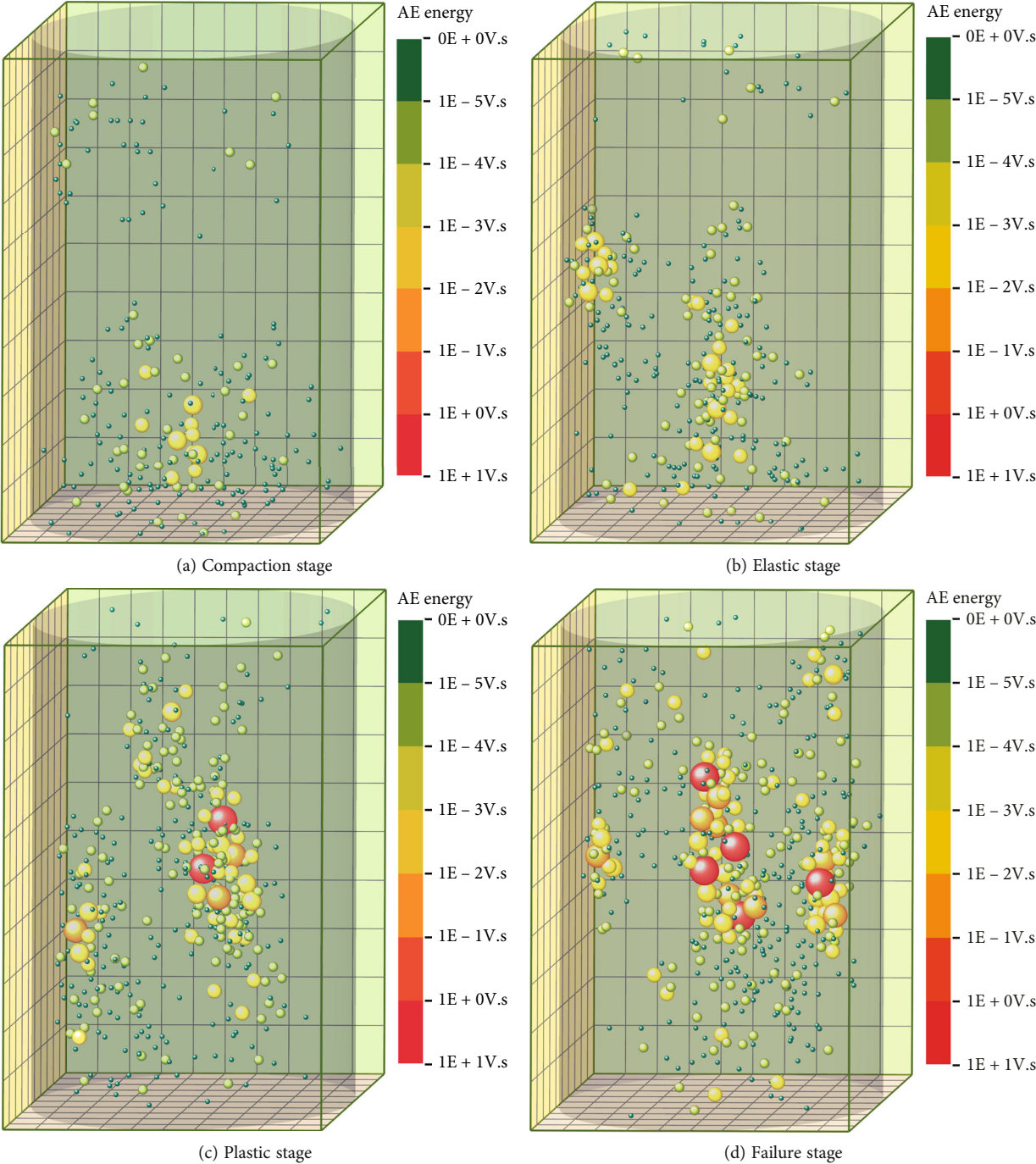


FIGURE 6: Continued.

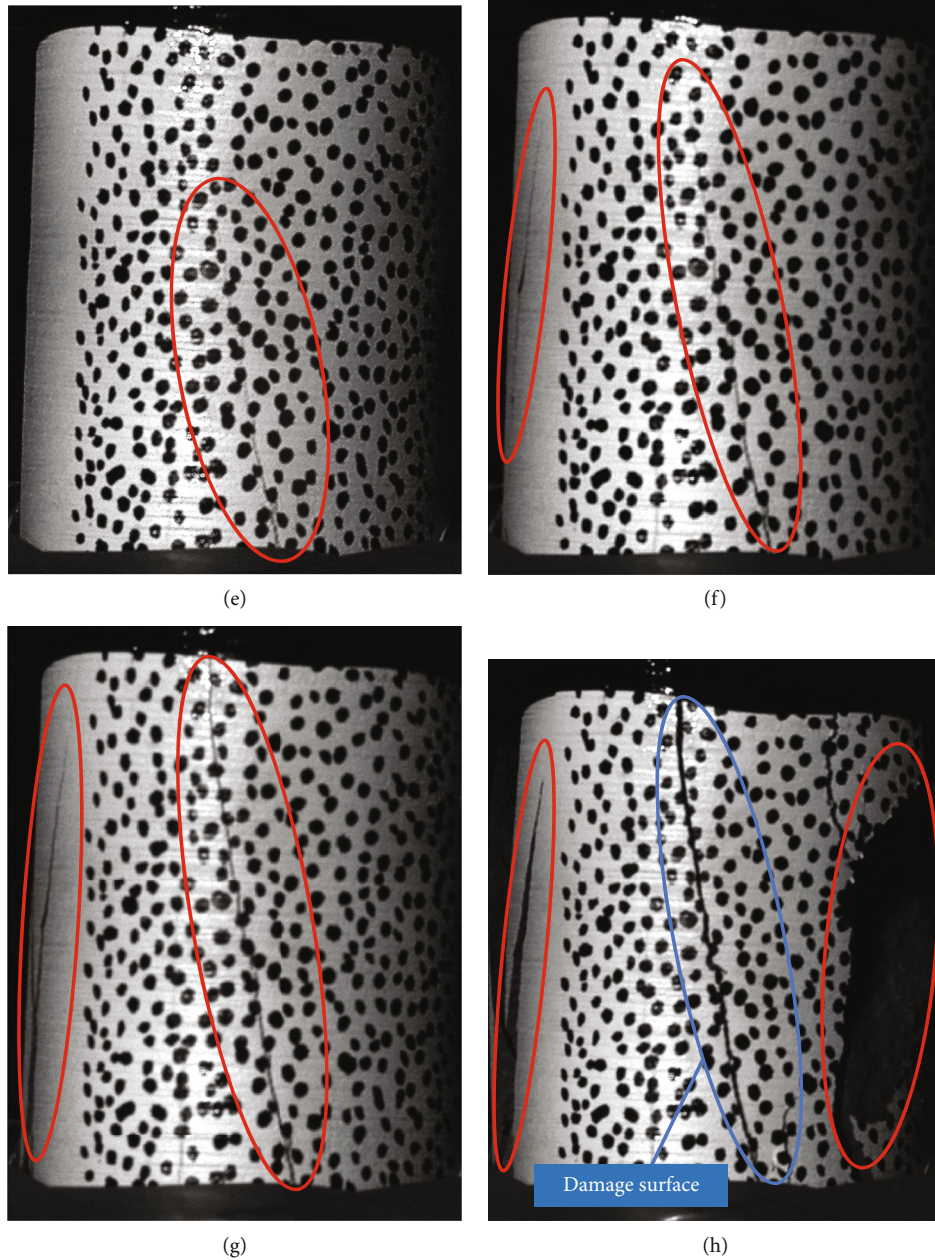


FIGURE 6: (a~d) AE source location and spatial evolution of rock sample U0-1 at different loading stages. (e~h) Physical images corresponding to the AE source location at different loading stages.

and lower ends of the specimen. The rock sample T7-1 has fewer positioning points and lower energy levels, the damaged surface is broken and consists of multiple cracks staggered, and five orange AE sources distribute in the upper part of the specimen where the damage is more serious.

Through the acoustic emission localization points and physical images inside the rock sample (Figures 5–8), it is found that the failure of the sample was a whole process of microcracks generating, expanding, and penetrating to form the damaged surface to instability. The release of energy always accompanies the development of rock cracks, so the AE positioning points often cluster near the cracks with the potential to expand or the penetrating damage surface.

The more energy the rock sample releases, the more serious the internal damage. Natural rock samples have many AE positioning points and high energy levels. The natural rock samples have strong intercrystal cohesion and a complete load-bearing skeleton, and microcracks can stably expand into large-scale cracks. When loaded to the peak stress, the large-scale cracks in the natural rock sample expand into a macroscopic damage surface, the elastic potential energy accumulated in the interior is released instantly, and the rock sample undergoes brittle failure accompanied by a loud and crisp sound. The water-saturated rock samples have several AE positioning points and low energy levels. Due to the water-rock chemistry of clay minerals (kaolinite and illite in

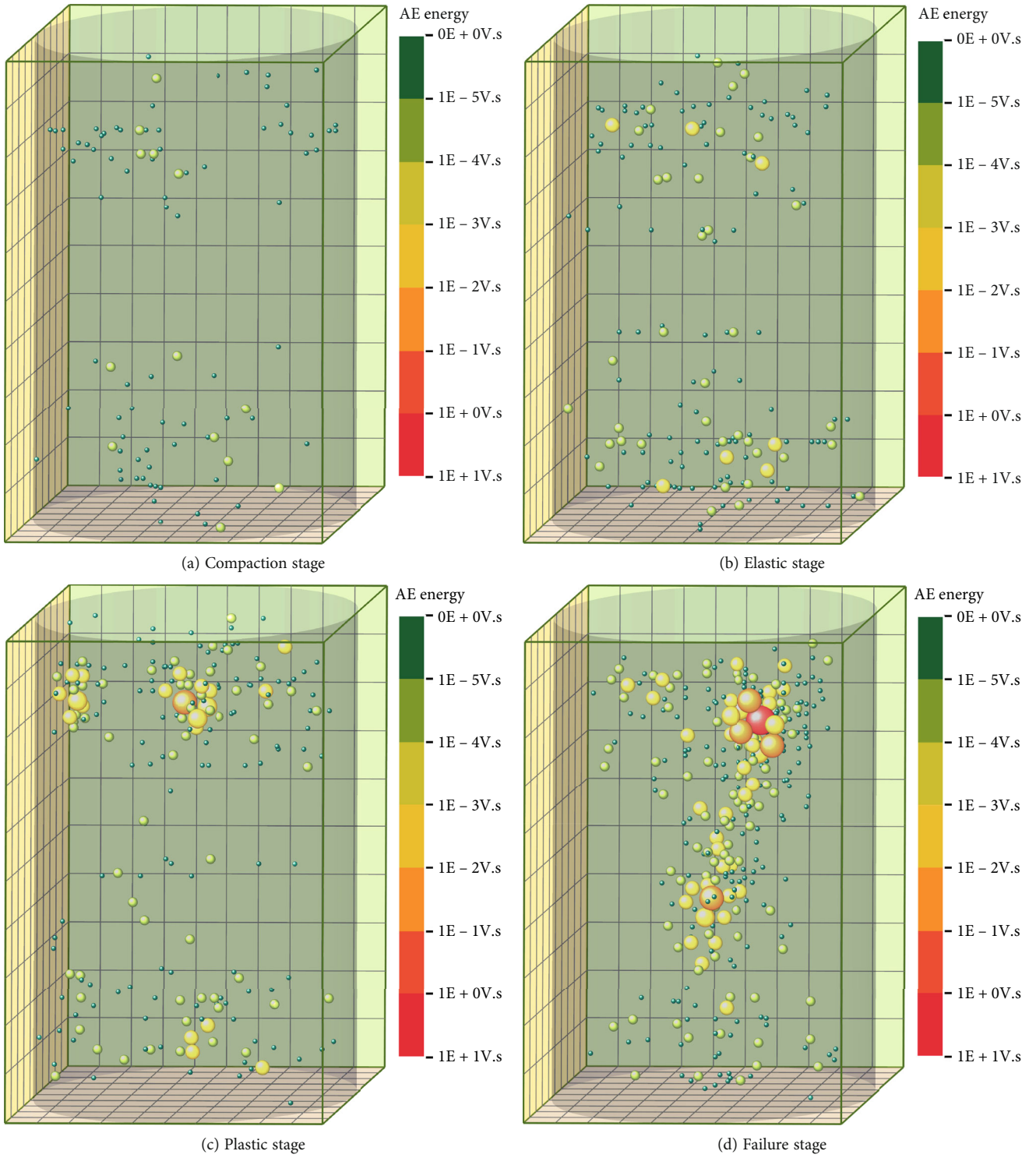


FIGURE 7: Continued.

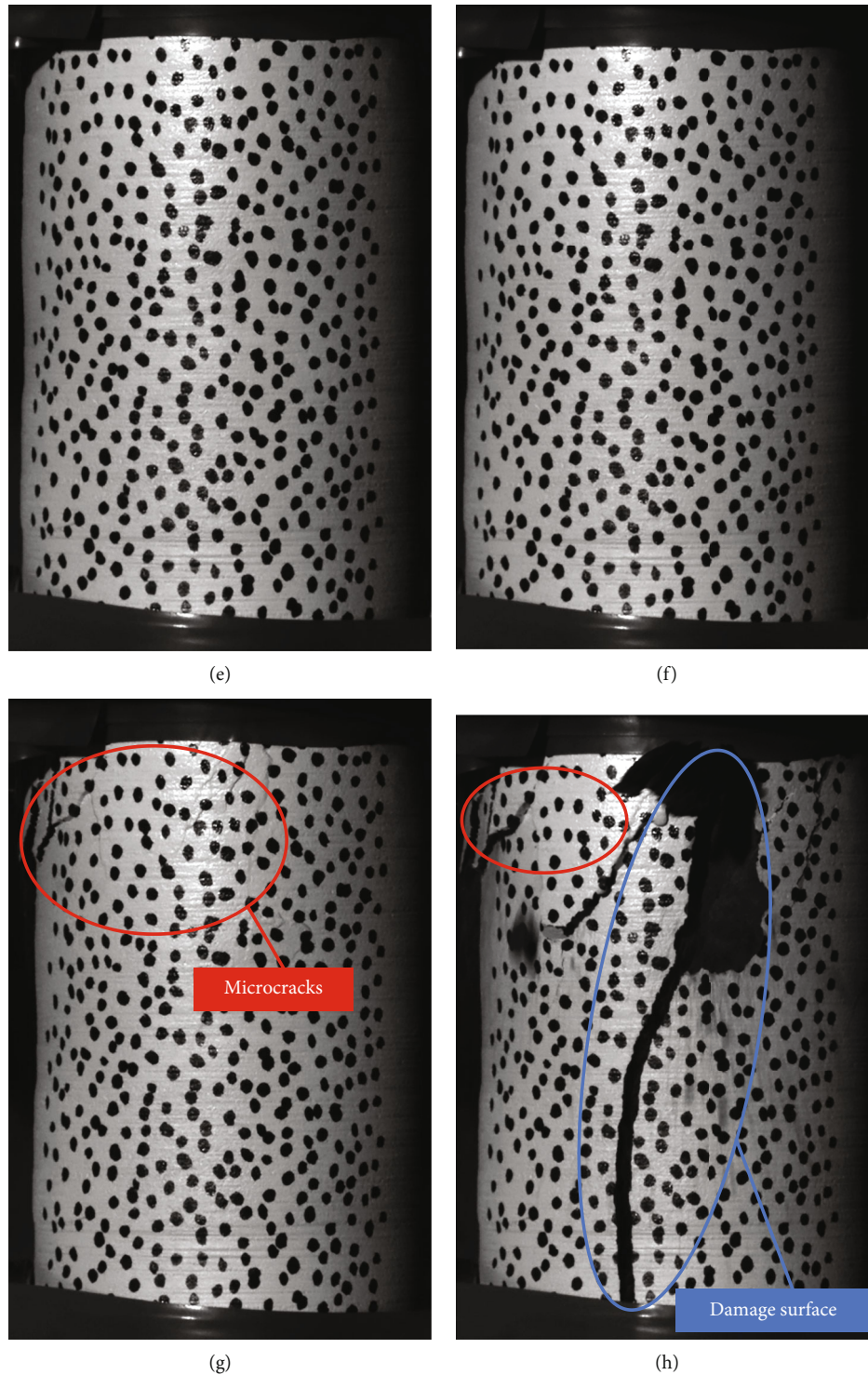


FIGURE 7: (a~d) AE source location and spatial evolution of rock sample U7-2 at different loading stages. (e~h) Physical images corresponding to the AE source location at different loading stages.

Figure 1), the intergranular structure is adjusted in the saturated rock sample, which expands the scale of primary cracks and microcracks in the rock sample and reduces the internal cementation force in the rock sample. When loaded to the peak stress, the microcracks inside the water-saturated rock sample expanded into large-scale cracks in a short time and penetrated the specimen to form the damaged surface,

and the rock sample suffered ductile failure accompanied by a fine and dense sound.

In summary, the crack of natural rock samples has a complete crack development process that can run through the whole loading stage. The cracks of water-saturated rock samples rapidly expand before failure and instability, forming macrodamage surfaces with more extensive scale and

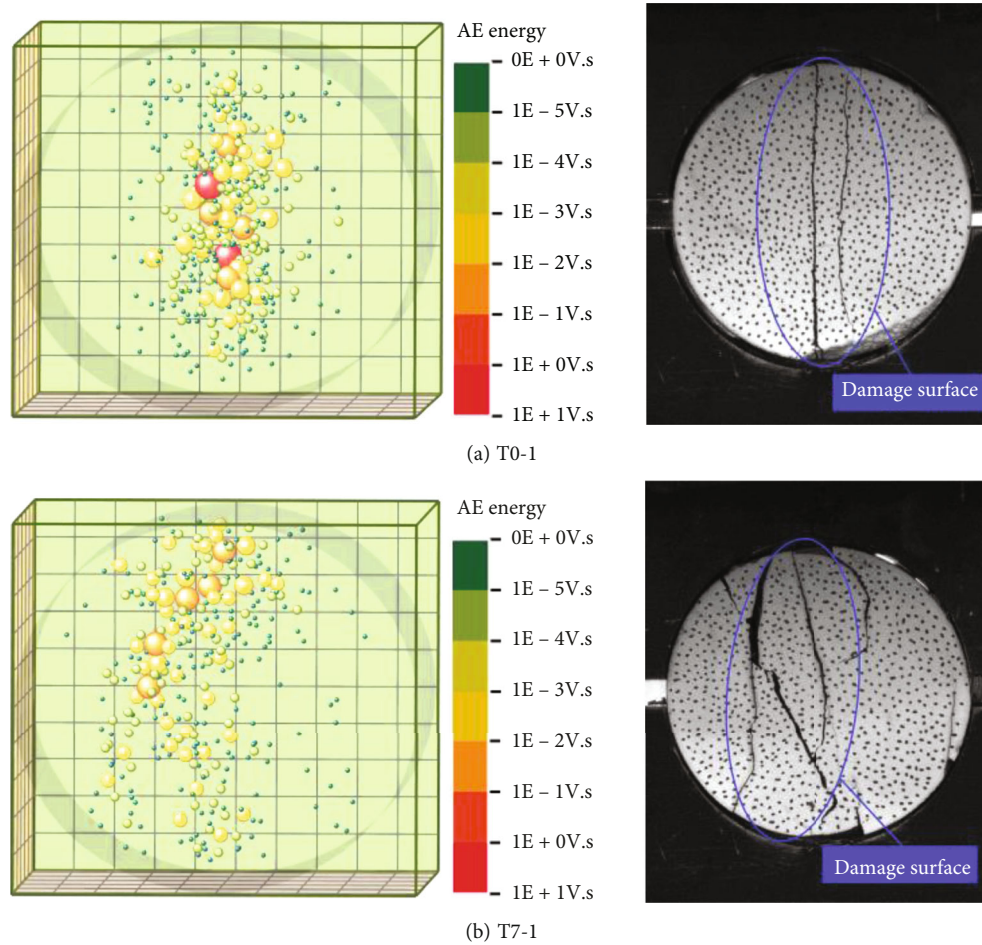


FIGURE 8: AE source location of rock samples and physical images in Brazilian indirect tensile test.

microcracks. Therefore, attention should be paid to monitoring damage accumulation in water-saturated rock mass in engineering practice.

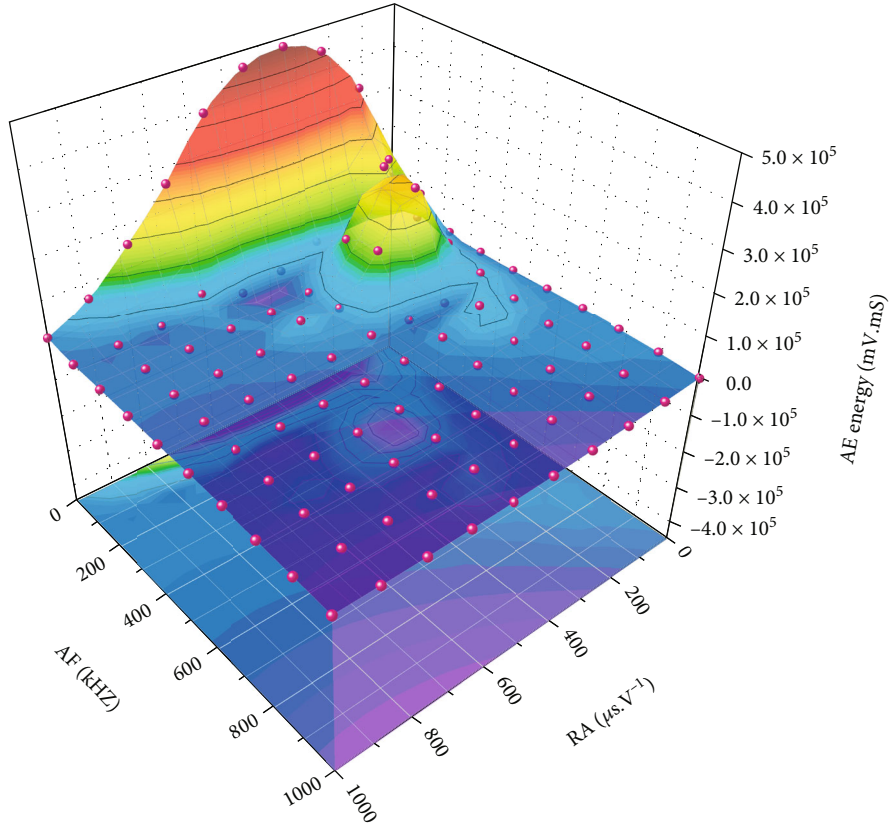
3.4. AF-RA-Energy Distribution. The acoustic emission signal will be generated during the deformation and failure. The failure modes and the crack propagation mechanisms can be better studied by analyzing the acoustic emission signal. Different types of cracks correspond to different acoustic emission waveforms. Tensile cracks have lower RA values and higher average frequency AF values, while shear cracks have higher RA values and lower AF values. Lower RA and AF values correspond to tensile-shear mixed cracks [32]. The RA and AF values are calculated using the acoustic emission amplitude and the acoustic emission ringing count received by the acoustic emission sensor. Combined with the energy parameters in acoustic emission, the three-dimensional correlation diagram of AF-RA-Energy is drawn to analyze the crack generation of rocks under different moisture contents.

The analysis results of the uniaxial compression test are shown in Figures 9(a) and 9(b); most of the AE signals have a wide range of RA value distribution (100~800 kHz) and low AF value (mostly 0-100 $\mu\text{s}/\text{V}$). Some acoustic emission signals are distributed in the low RA (200~400 $\mu\text{s}/\text{V}$) range

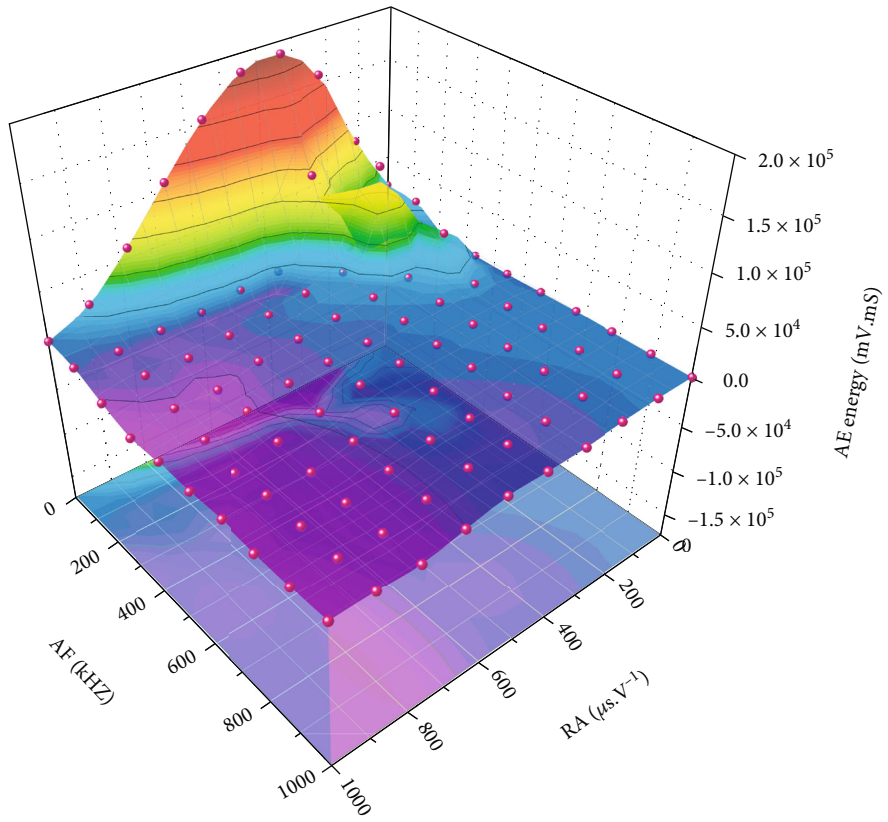
and low AF (200~400 kHz) range. The distribution characteristics of the natural rock sample U0-1 and the saturated rock sample U7-2 are similar. Still, the acoustic emission energy value of sample U0-1 is higher, and the distribution range is broader than that of sample U7-2 (U0-1 is 100~700 $\mu\text{s}/\text{V}$ and 200~600 $\mu\text{s}/\text{V}$ for U7-2).

The Brazilian indirect tensile test analysis results are shown in Figures 9(c) and 9(d). The two rock samples' acoustic emission signals are similar, indicating a low RA value (0-400 $\mu\text{s}/\text{V}$) and a wide distribution of AF value (1000 kHz). The acoustic emission energy values of natural rock sample T0-1 and saturated rock sample T7-1 are similar. The higher acoustic emission energy values are concentrated in the range of 0-100 $\mu\text{s}/\text{V}$ for RA and 200-600 kHz for AF.

Therefore, shear cracks and mixed tensile-shear cracks occurred in the uniaxial compression test, and the shear cracks dominated and led to the shear failure of the rock samples. Tensile cracks dominated the rock samples in the Brazilian indirect tensile experiment, and a tensile-dominated failure occurred. From Figures 9(a)–9(d), it can be seen that the AE energy values are more prominent in shear-dominated failure than in tensile-dominated failure. This indicates that microcracks' initiation and propagation activities are more intense in shear failure than in tensile

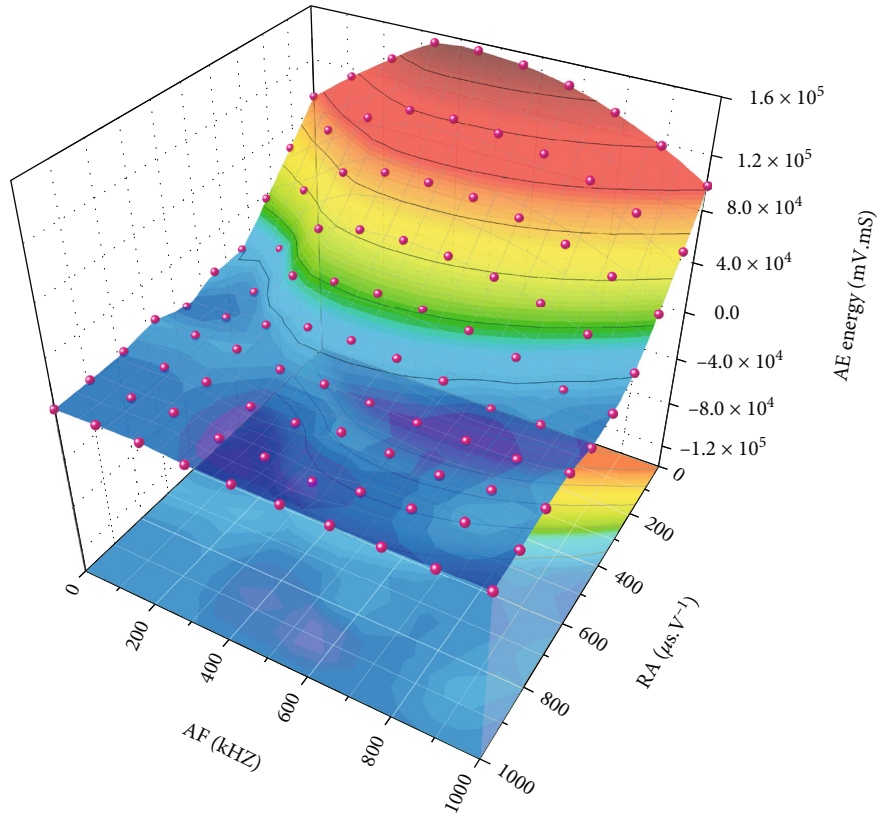


(a) U0-1

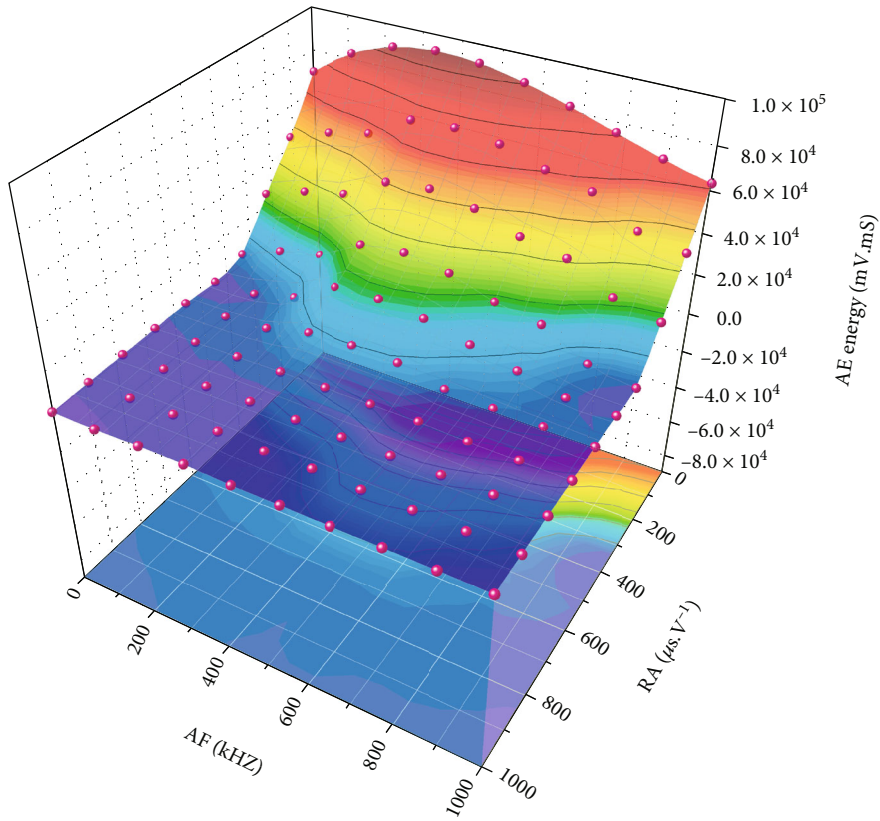


(b) U7-2

FIGURE 9: Continued.



(c) T0-1



(d) T7-1

FIGURE 9: Three-dimensional correlation plot of the AE parameters. (a, b) Uniaxial compression test. (c, d) Brazilian indirect tensile test.

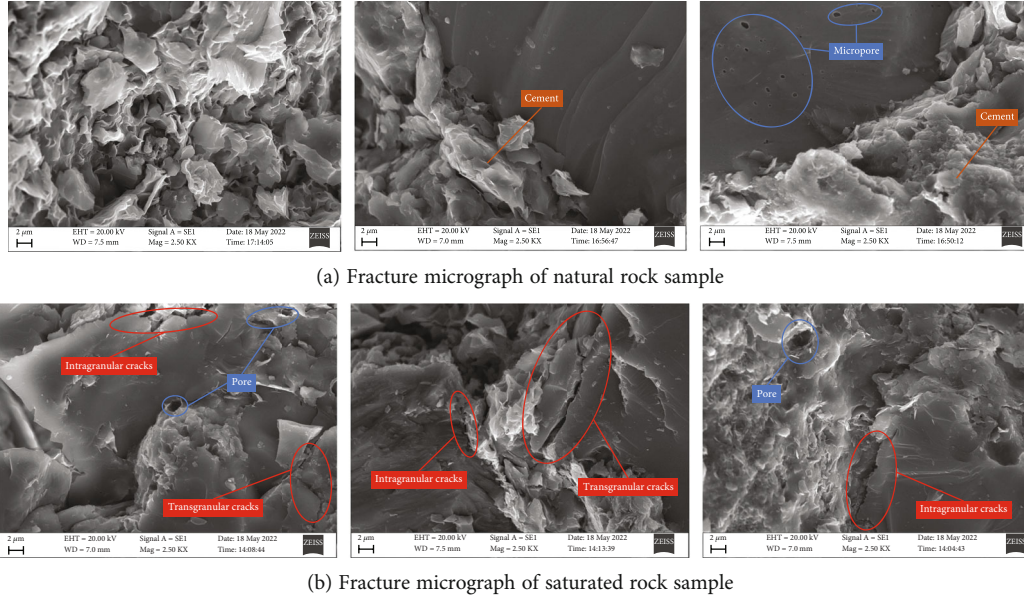


FIGURE 10: Typical microstructure of argillaceous siltstone fracture.

failure, resulting in more released elastic strain energy. With the increase of moisture content, the elastic strain energy released by rock sample failure gradually attenuates.

4. Microstructure Analysis of Fracture

In order to analyze the crack propagation mechanisms of argillaceous siltstone under different moisture content, the fracture surfaces of natural and saturated samples were examined by SEM. Clean rock fracture fragments of appropriate size are selected to process the standard block samples. Figures 10(a) and 10(b) are typical fracture micrographs of argillaceous siltstone specimens under different moisture contents. The results show that the microstructure of argillaceous siltstone is composed of a single random accumulation of mineral particles and a certain amount of illite, plagioclase, clay minerals, and pores. Clay minerals contain 5% chlorite and 10% hydromica/illite. Although the composition of clay minerals is relatively low, it promotes the chemical interaction between water and rock to a certain extent. In addition, the argillaceous siltstone presents a mode of pore cementation of microstructure. The cementing substances are mainly 5% calcite (carbonate mineral) and a small amount of iron oxide, which is distributed along the filling between the mineral grains, whereas in carbonate minerals, the adsorption of ion exchange and soluble cementing substances can lead to a more sensitive water-rock chemistry in argillaceous siltstones [33].

In contrast, it is not difficult to see that the natural rock samples maintain uniform mineral particles and regular shapes after tensile and shear failure. The cementing substances are tightly surrounded by the particles and are neat and dense, with few pores and cracks. Clay minerals tend to block pore throats and increase the cohesion between mineral particles [34, 35]. As the moisture content increases, the mineral particles gradually loosen. The cementing substances and clay minerals undergo water-rock chemistry,

causing the mineral particles to dissolve along the joints and produce transgranular cracks. The cementing substances dissolve, and the mineral particles begin to break away from the connection of the cementing substances, resulting in intercrystalline cracks and large-scale dissolution pores. In other words, intergranular cracks, transgranular cracks, and large-scale pores are more likely to promote the initiation and propagation of microcracks. From the above analysis, it is clear that the water-rock chemistry of the argillaceous siltstone is not negligible.

For argillaceous siltstone, the cohesion between the interstices of the clastic material is much smaller than the strength of the mineral particles, and there is no good interlocking between the mineral particles. The chemical interaction between water and rock intensifies the dissolution phenomenon and contributes to the initiation and propagation of microcracks. Therefore, the strength of argillaceous siltstone is determined by the cohesion of the cementitious material. This is why water-saturated rock samples have more microcracks and lower strength than natural rock samples.

5. Fractal Characteristics of AE Time Sequence

The time sequence characteristic parameters in rock acoustic emission signals can be regarded as a set of univariate time series with obvious fractal characteristics [26]. This study adopts the G-P algorithm [36, 37] proposed by Grassberger and Procaccia based on the embedding theory and the idea of reconstructed phase space to calculate the correlation dimension from the time series. Taking the primary parameter sequence of the acoustic emission process as the research object, the primary parameter sequence of each acoustic emission process can correspond to a series set with a capacity of n :

$$X = \{x_1, x_2, \dots, x_n\}. \quad (1)$$

According to formula (1), an m -dimensional phase space ($m < n$) can be constructed, and the number of m paralleled in it is selected as the first vector of the m -dimensional space:

$$X_1 = \{x_1, x_2, \dots, x_m\}. \quad (2)$$

Then, translate one piece of data to the right and take m numbers to form the second vector:

$$X_2 = \{x_2, x_3, \dots, x_{m+1}\}. \quad (3)$$

By analogy, N ($N = n - m + 1$) vectors can be formed, and the corresponding correlation function is

$$C(r) = \frac{1}{N^2} \cdot \sum_{i=1}^N \sum_{j=1}^N H[r - |x_i - x_j|], \quad (4)$$

where H is the Heaviside function, and its expression is

$$H(u) = \begin{cases} 0, & u < 0, \\ 1, & u \geq 0. \end{cases} \quad (5)$$

In order to avoid dispersion when giving the value of r , the value of r is

$$r = kr_0. \quad (6)$$

In formula (6), k is the proportional coefficient, and r_0 is

$$r_0 = \frac{1}{N^2} \cdot \sum_{i=1}^N \sum_{j=1}^N |x_i - x_j|. \quad (7)$$

According to formulas (1)-(7), n points can be obtained. Plot it in double logarithmic coordinates and fit it. If the fitting result is a straight line, it means that the acoustic emission series has fractal properties in the given scale range, and the correlation dimension is the slope of the straight line.

$$D = \frac{\lg C(r)}{\lg r}. \quad (8)$$

Figure 11 shows the $\ln C(r) - \ln r$ curves for different values of m , the scale r remains constant, and the slope of the double logarithmic curve gradually increases as the value of m increases. As shown in Figure 12, after $m = 6$, the increase of the slope tends to be gentle, and the correlation dimension begins to stabilize. Therefore, the value of the phase space dimension is chosen to be 6 for calculation in this paper.

For representative rock samples with different moisture contents, the AE signal parameters collected under the uniaxial compression test and the Brazilian indirect tensile test were used to calculate the correlation dimension by the G-P algorithm. There are very few AE signals early in the failure stage, and it is impossible to calculate the correlation dimension in the case of relatively low failure stress. Therefore, the AE signal is selected after the relative failure stress of 30%. The relationship between the correlation dimension and the

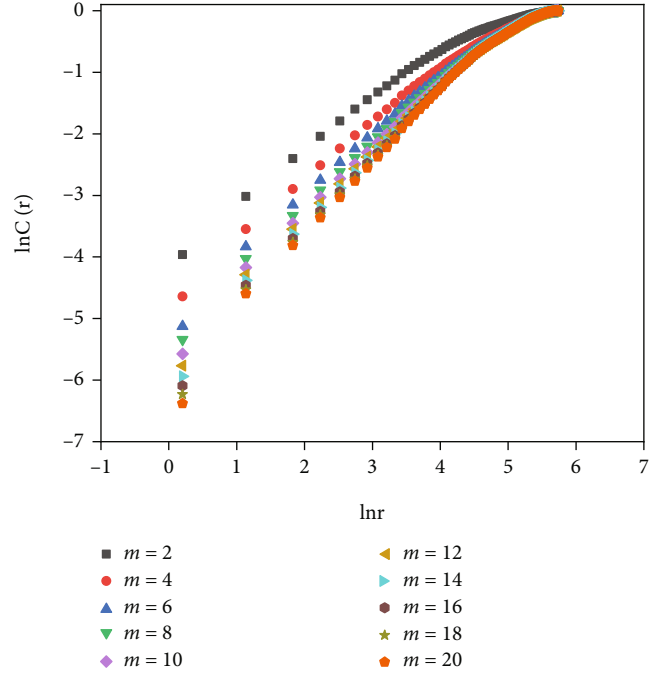


FIGURE 11: The $\ln C(r) - \ln r$ correlation for different m values.

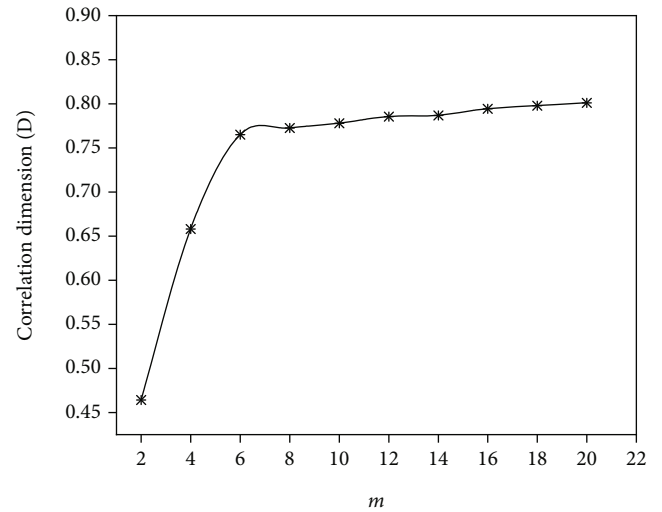


FIGURE 12: The relationship between correlation dimension D and parameter m .

relative failure stress of rock samples with different moisture contents under the two tests is obtained, as shown in Figure 13.

The results show that the AE fractal dimension D values under different moisture contents are more significant at around 40% of the relative failure stress. The overall variation in the curve shows a decreasing trend. In the early loading stage, the relative failure stress level is low, and the AE signal is sparse and stray. The AE time sequence produced less energy and larger intervals, resulting in higher fractal dimension D values within 0.5 to 0.7. As the stress increases, the specimen enters the elastic stage, the acoustic emission

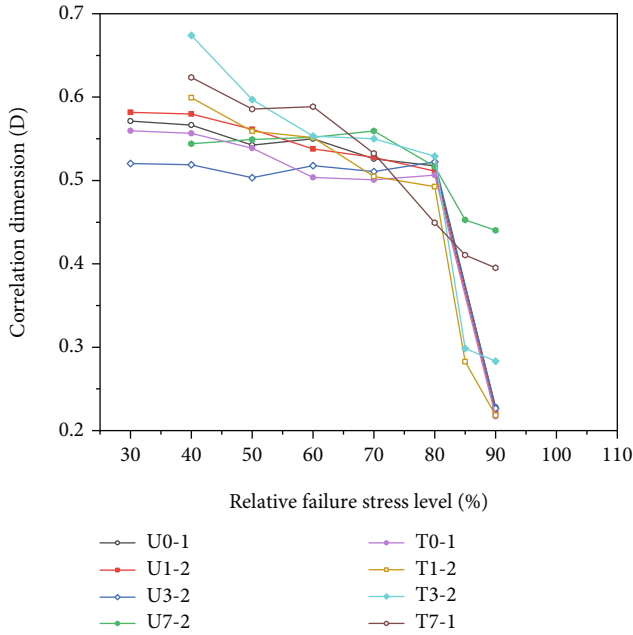


FIGURE 13: Relationships between stress percentages and correlation dimension values for different moisture contents.

event is localized, and the AE positioning points are concentrated in the damaged part of the specimen (as shown in Figures 6–8), resulting in a slight decrease in the fractal dimension D value. Under higher stress conditions, large-scale cracks propagate through the entire specimen to form a damaged surface, and high-level AE positioning points are clustered near the damaged surface. AE events are spatially centralized, which is the ordering of rupture damage. The elastic strain energy accumulated in the specimen is released instantaneously when the stress peak is reached, resulting in the generation of a large number of high-level AE events and shortening the interval of the AE time sequence. The fractal dimension D value dropped abruptly to a minimum value, and all stabilized at a similar level, around 0.25.

The fractal dimension D value also varies with the moisture content. The D value of the specimen with lower moisture content gradually decreased with the stress and dropped abruptly to around 0.25 near the peak value. The more significant decrease of the fractal dimension D value indicates that the critical AE events increase sharply, the energy released by the failure is more prominent, and the cracks formed are less complicated. The D value of specimen U7-2 with higher moisture content increases slowly with the stress, decreases when it is close to the peak stress, and stabilizes around 0.45. The D value of specimen T7-1 varies from 0.4 to 0.65. When the specimens with higher moisture content are damaged, the fractal dimension D value is finally stable above 0.4. This shows that when the moisture content of the specimen is taller, the number of microcracks will be, and the way of propagation is more complicated. Finally, the microcrack will expand into multiple microcrack branches. This is because hydration adjusts the structure of crystal grains inside the rock sample, and the rock sample loses part

of the cementation force, which makes it easier for cracks to expand further.

It can be seen from the above analysis that the time sequence characteristic parameters in the AE signal in the whole process of argillaceous siltstone failure under different moisture contents have fractal characteristics. The variation in the fractal dimension D value gives a good indication of the order and complexity of the crack propagation, thus understanding the state and development of damage within the rock sample.

6. Conclusions

The AE characteristics of argillaceous siltstone with different moisture contents in the uniaxial compression test and Brazilian indirect tensile test were analyzed by AE detection technology. The relationship between AE spatial distribution, failure mode, crack type, fractal dimension, and moisture content was studied. The research results can support monitoring rock mass stability under different water-bearing conditions.

- (1) The moisture content has a significant influence on the strength of argillaceous siltstone. The peak tensile and compressive strengths of natural rock samples were the largest among all specimens. With the increase of moisture content, the rock strength gradually decreases. When the moisture content reaches about 1.7292%, the rock sample reaches saturation, and the peak intensity is the smallest
- (2) AE activities showed different characteristics under the two experiments, but the frequency and intensity of acoustic emission activities showed a decreasing trend with the increase of moisture content. In the AE signal in uniaxial compression test, the peak frequency is mainly distributed below 100 kHz. A large amount of energy is released during instability failure, and high-energy AE sources cluster near the failure surface, forming high RA-low AF shear cracks and low RA-low AF tensile-shear mixed cracks. In the AE signal in Brazilian indirect tensile test, the peak frequency is mainly distributed in 200–400 kHz. AE sources clustered near the fracture surface have lower energy levels and fewer numbers and form tensile cracks with low RA and high AF during failure
- (3) SEM and XRD results show a certain amount of clay minerals in the argillaceous siltstone that can undergo water-rock chemistry. The microstructure of the fracture of the natural specimen is neat and dense. With the increase in moisture content, mineral particles and cemented substances are eroded, and transgranular cracks, intergranular cracks, and large-scale pores mainly characterize the microstructure of the fracture. Therefore, water-saturated specimens are more likely to generate microcracks with the potential to expand

- (4) The AE fractal dimension showed a decreasing trend with the increase of the relative failure stress. The fractal dimension of the specimen with lower moisture content dropped at the peak stress and stabilized around 0.25. The fractal dimension of water-saturated specimens varies from 0.4 to 0.65. This indicates that the number of microcracks will be more, and the expansion will be more complex when the water-saturated specimens are damaged, which is consistent with the evolution patterns of the acoustic emission localization source

Data Availability

The data that support the findings of this study are available from the corresponding author upon reasonable request.

Conflicts of Interest

The authors declare that they have no conflicts of interest.

Acknowledgments

The authors are grateful to the staffs from The Fifth Engineering Co., Ltd. of China Railway First Engineering Group, for their kindly assistance in the collection of argillaceous siltstone samples. This study was supported by the Key R&D Program of Yunnan Provincial Department of Science and Technology (2018BC008), the National Natural Science Foundation of China (51768065), the Science and Technology Development Project of China Railway Co., Ltd. (XLKK-333-2021-024), and the China Railway Science and Technology Research and Development Program (2020-Major Special-04).

References

- [1] G. Zhang, L. Chen, Z. Wen et al., "Squeezing failure behavior of roof-coal masses in a gob-side entry driven under unstable overlying strata," *Energy Science & Engineering*, vol. 8, no. 7, pp. 2443–2456, 2020.
- [2] Y. Wang, Y. Su, Y. Xia, H. Wang, and X. Yi, "On the effect of confining pressure on fatigue failure of block-in-matrix soils exposed to multistage cyclic triaxial loads," *Fatigue & Fracture of Engineering Materials & Structures*, vol. 45, no. 9, pp. 2481–2498, 2022.
- [3] Y. Wang, P. Tang, J. Han, and P. Li, "Energy-driven fracture and instability of deeply buried rock under triaxial alternative fatigue loads and multistage unloading conditions: prior fatigue damage effect," *International Journal of Fatigue*, vol. 168, article 107410, 2023.
- [4] X. Cai, Z. Zhou, and D. Xueming, "Water-induced variations in dynamic behavior and failure characteristics of sandstone subjected to simulated geo-stress," *International Journal of Rock Mechanics and Mining Sciences*, vol. 130, p. 104339, 2020.
- [5] A. Basu, D. A. Mishra, and K. Roychowdhury, "Rock failure modes under uniaxial compression, Brazilian, and point load tests," *Bulletin of Engineering Geology and the Environment*, vol. 72, no. 3-4, pp. 457–475, 2013.
- [6] P. F. Wu, W. G. Liang, Z. G. Li, M. T. Cao, and J. F. Yang, "Investigations on mechanical properties and crack propagation characteristics of coal and sandy mudstone using three experimental methods," *Rock Mechanics and Rock Engineering*, vol. 50, no. 1, pp. 215–223, 2017.
- [7] S. Okubo, K. Fukui, and Q. Qingxin, "Uniaxial compression and tension tests of anthracite and loading rate dependence of peak strength," *International Journal of Coal Geology*, vol. 68, no. 3-4, pp. 196–204, 2006.
- [8] T. Guo, S. Zhang, H. Ge, X. Wang, X. Lei, and B. Xiao, "A new method for evaluation of fracture network formation capacity of rock," *Fuel*, vol. 140, pp. 778–787, 2015.
- [9] R. Vidya Sagar and M. V. M. S. Rao, "An experimental study on loading rate effect on acoustic emission based *b*-values related to reinforced concrete fracture," *Construction and Building Materials*, vol. 70, pp. 460–472, 2014.
- [10] S. Xu, J.-p. Liu, S.-d. Xu, J. Wei, W.-b. Huang, and L.-b. Dong, "Experimental studies on pillar failure characteristics based on acoustic emission location technique," *Transactions of Nonferrous Metals Society of China*, vol. 22, no. 11, pp. 2792–2798, 2012.
- [11] X. Kong, E. Wang, S. Hu, R. Shen, X. Li, and T. Zhan, "Fractal characteristics and acoustic emission of coal containing methane in triaxial compression failure," *Journal of Applied Geophysics*, vol. 124, pp. 139–147, 2016.
- [12] J. Guo, P. Liu, J. Fan, and H. Zhang, "Study on the mechanical behavior and acoustic emission properties of granite under triaxial compression," *Geofluids*, vol. 2021, Article ID 3954097, 17 pages, 2021.
- [13] A. Lisjak, G. Grasselli, and T. Vietor, "Continuum-discontinuum analysis of failure mechanisms around unsupported circular excavations in anisotropic clay shales," *International Journal of Rock Mechanics and Mining Sciences*, vol. 65, pp. 96–115, 2014.
- [14] X. Xu, L. Dou, C. Lu, and Y. Zhang, "Frequency spectrum analysis on micro-seismic signal of rock bursts induced by dynamic disturbance," *Mining Science and Technology (China)*, vol. 20, no. 5, pp. 682–685, 2010.
- [15] W. Blake, *Microseismic Applications for Mining: A Practical Guide [M]*, US Department of the Interior, Bureau of Mines, 1982.
- [16] C. Zhang, G. Jin, C. Liu et al., "Prediction of rockbursts in a typical island working face of a coal mine through microseismic monitoring technology," *Tunnelling and Underground Space Technology*, vol. 113, p. 103972, 2021.
- [17] H. Wang, D. Liu, Z. Cui, C. Cheng, and Z. Jian, "Investigation of the fracture modes of red sandstone using XFEM and acoustic emissions," *Theoretical and Applied Fracture Mechanics*, vol. 85, pp. 283–293, 2016.
- [18] S. W. Zhang, K. J. Shou, X. F. Xian, J. P. Zhou, and G. J. Liu, "Fractal characteristics and acoustic emission of anisotropic shale in Brazilian tests," *Tunnelling and Underground Space Technology*, vol. 71, pp. 298–308, 2018.
- [19] D.-S. Cheon, Y.-B. Jung, E.-S. Park, W. K. Song, and H. I. Jang, "Evaluation of damage level for rock slopes using acoustic emission technique with waveguides," *Engineering Geology*, vol. 121, no. 1-2, pp. 75–88, 2011.
- [20] Y. Wang, H. Deng, Y. Deng, K. Chen, and J. He, "Study on crack dynamic evolution and damage-fracture mechanism of rock with pre-existing cracks based on acoustic emission location," *Journal of Petroleum Science and Engineering*, vol. 201, p. 108420, 2021.

- [21] J. Liu, N. Wu, G. Si, and M. Zhao, "Experimental study on mechanical properties and failure behaviour of the pre-cracked coal-rock combination," *Bulletin of Engineering Geology and the Environment*, vol. 80, no. 3, pp. 2307–2321, 2020.
- [22] S.-Q. Yang, H.-W. Jing, and S.-Y. Wang, "Experimental investigation on the strength, deformability, failure behavior and acoustic emission locations of red sandstone under triaxial compression," *Rock Mechanics and Rock Engineering*, vol. 45, no. 4, pp. 583–606, 2012.
- [23] L. G. Tham, H. Liu, C. A. Tang, P. K. K. Lee, and Y. Tsui, "On tension failure of 2-D rock specimens and associated acoustic emission," *Rock Mechanics and Rock Engineering*, vol. 38, no. 1, pp. 1–19, 2004.
- [24] K. Kusunose, X. Lei, O. Nishizawa, and T. Satoh, "Effect of grain size on fractal structure of acoustic emission hypocenter distribution in granitic rock," *Physics of the Earth and Planetary Interiors*, vol. 67, no. 1–2, pp. 194–199, 1991.
- [25] H. P. Xie, J. F. Liu, Y. Ju, J. Li, and L. Z. Xie, "Fractal property of spatial distribution of acoustic emissions during the failure process of bedded rock salt," *International Journal of Rock Mechanics and Mining Sciences*, vol. 48, no. 8, pp. 1344–1351, 2011.
- [26] M. Biancolini, C. Brutti, G. Paparo, and A. Zanini, "Fatigue cracks nucleation on steel, acoustic emission and fractal analysis," *International Journal of Fatigue*, vol. 28, no. 12, pp. 1820–1825, 2006.
- [27] R. Zhang, F. Dai, M. Z. Gao, N. W. Xu, and C. P. Zhang, "Fractal analysis of acoustic emission during uniaxial and triaxial loading of rock," *International Journal of Rock Mechanics and Mining Sciences*, vol. 79, pp. 241–249, 2015.
- [28] V. A. Akinbinu, "Multivariate analysis of fracture toughness, brittleness and blasting geometric ratios for the prediction of fragmentation output," *International Journal of Rock Mechanics and Mining Sciences*, vol. 93, pp. 324–329, 2017.
- [29] Y. Wang, T. Mao, Y. Xia, X. Li, and X. Yi, "Macro-meso fatigue failure of bimrocks with various block content subjected to multistage fatigue triaxial loads," *International Journal of Fatigue*, vol. 163, p. 107014, 2022.
- [30] Y. Wang, Z. Y. Song, T. Q. Mao, and C. Zhu, "Macro-meso fracture and instability behaviors of hollow-cylinder granite containing fissures subjected to freeze-thaw-fatigue loads," *Rock Mechanics and Rock Engineering*, vol. 55, no. 7, pp. 4051–4071, 2022.
- [31] Z. Cuiying, D. Yimei, and T. Xiangshao, "Experimental research on the softening of mechanical properties of saturated soft rocks and application," *Chinese Journal of Rock Mechanics and Engineering*, vol. 24, no. 1, pp. 33–38, 2005, (in Chinese).
- [32] K. Du, X. Li, M. Tao, and S. Wang, "Experimental study on acoustic emission (AE) characteristics and crack classification during rock fracture in several basic lab tests," *International Journal of Rock Mechanics and Mining Sciences*, vol. 133, p. 104411, 2020.
- [33] Z. H. A. O. Kui, R. A. N. Shanhu, and Z. E. N. G. Peng, "Effect of moisture content on characteristic stress and acoustic emission characteristics of red sandstone," *Rock and Soil Mechanics*, vol. 42, no. 4, pp. 899–908, 2021.
- [34] J. Kantorowicz, "The influence of variations in illite morphology on the permeability of Middle Jurassic Brent Group sandstones, Cormorant Field, UK North Sea," *Marine and Petroleum Geology*, vol. 7, no. 1, pp. 66–74, 1990.
- [35] R. Worden and S. Morad, "Quartz cementation in oil field sandstones: a review of the key controversies," in *Quartz Cementation in Sandstones*, pp. 1–20, Wiley, 2009.
- [36] P. Grassberger, "Generalized dimensions of strange attractors," *Physics Letters A*, vol. 97, no. 6, pp. 227–230, 1983.
- [37] P. Grassberger and I. Procaccia, "Measuring the strangeness of strange attractors," *Physica D: Nonlinear Phenomena*, vol. 9, no. 1–2, pp. 189–208, 1983.